Chemical Science

ROYAL SOCIETY OF CHEMISTRY

EDGE ARTICLE

View Article Online
View Journal | View Issue

Cite this: *Chem. Sci.*, 2021, **12**, 1433

All publication charges for this article have been paid for by the Royal Society of Chemistry

Mechanism of inhibition of SARS-CoV-2 M^{pro} by N3 peptidyl Michael acceptor explained by QM/MM simulations and design of new derivatives with tunable chemical reactivity†

Kemel Arafet, [a] Natalia Serrano-Aparicio, [a] Alessio Lodola, [b] Adrian J. Mulholland, [c] Florenci V. González, [d] Katarzyna Świderek *[a] and Vicent Moliner *[a]

Received 10th November 2020
Accepted 26th November 2020

DOI: 10.1039/d0sc06195f

rsc.li/chemical-science

The SARS-CoV-2 main protease (M^{pro}) is essential for replication of the virus responsible for the COVID-19 pandemic, and one of the main targets for drug design. Here, we simulate the inhibition process of SARS-CoV-2 M^{pro} with a known Michael acceptor (peptidyl) inhibitor, **N3**. The free energy landscape for the mechanism of the formation of the covalent enzyme-inhibitor product is computed with QM/MM molecular dynamics methods. The simulations show a two-step mechanism, and give structures and calculated barriers in good agreement with experiment. Using these results and information from our previous investigation on the proteolysis reaction of SARS-CoV-2 M^{pro}, we design two new, synthetically accessible **N3**-analogues as potential inhibitors, in which the recognition and warhead motifs are modified. QM/MM modelling of the mechanism of inhibition of M^{pro} by these novel compounds indicates that both may be promising candidates as drug leads against COVID-19, one as an irreversible inhibitor and one as a potential reversible inhibitor.

Introduction

A novel coronavirus (severe acute respiratory syndrome coronavirus-2 – SARS-CoV-2) has been identified as responsible for the COVID-19 pandemic. There is a pressing need for effective antiviral treatments. Many researchers around the world are working to develop SARS-CoV-2 antiviral compounds, *e.g.* following previous SARS-CoV and MERS-CoV outbreaks and research. Remarkable progress has been achieved in just a few months with regard to the understanding of the phylogeny and genomic organization of SARS-CoV-2 as well as its molecular mechanisms of infection and replication.[1] Knowledge of the life cycle of SARS-CoV-2 provides information about possible targets for drug development.[2] These include inhibition of the viral–host interaction, endosome maturation, viral/endosome membrane fusion, and viral polypeptide maturation.[3] Intense work has focused on identification and testing of compounds already approved for the treatment of other diseases such as remdesivir, a drug developed previously against Ebola virus (EBOV),[4] dexamethasone and antimalarial drugs.[5] While some studies show promise, there is a clear need for new compounds, specific to SARS-CoV-2, both as drug leads and as biochemical probes.[6–9]

The present study focuses on the atomistic characterization of the inhibition mechanism of one of the proteins responsible for the virus replication and maturation, the main coronavirus protease (SARS-CoV-2 M^{pro}, also called 3CL^{pro}). M^{pro}, together with the papain-like protease PL^{pro}, are cysteine protease (CPs) that process the polyproteins that are translated from the viral RNA in the replication of the SARS-CoV-2 virus. Thus, inhibiting activity of these enzymes would block the viral life cycle. In addition, a distinguishing feature of SARS-CoV-2 M^{pro} with respect to human proteases is its ability to cleave peptides after a glutamine residue. This feature, which is shared also by SARS-CoV 3CL protease,[10] has prompted a search for inhibitors incorporating a glutamine residue/mimic in their structure (see below) with the aim of obtaining selectivity in addition to potency.[5] The current scenario explains recent efforts devoted to

[a]*Departament de Química Física i Analítica, Universitat Jaume I, 12071 Castelló, Spain. E-mail: swiderek@uji.es; moliner@uji.es*

[b]*Dipartimento di Scienze degli Alimenti e del Farmaco, Università degli Studi di Parma, Italy*

[c]*Centre for Computational Chemistry, School of Chemistry, University of Bristol, UK*

[d]*Departament de Química Inorgànica i Orgànica, Universitat Jaume I, 12071 Castelló, Spain*

† Electronic supplementary information (ESI) available: Computational methods, FF parameters for inhibitors, detail of active site and QM-MM partitioning, M06-2X:AM1/MM FESs, list of key interatomic distances in the states along the reaction path at AM1/MM and optimized at M06-2X/MM level, protein-substrate non-bonding interaction energies, per residue, Cartesian coordinates of the QM subset of atoms and full structures of the rate-limiting TSs, **E:I** and **E-I** optimized at M06-2X/6-31+G(d,p)/MM level, and figure of inhibitors docked into the active site of SARS-CoV-2 M^{pro}. See DOI: 10.1039/d0sc06195f

the identification of inhibitors of this enzyme, aided by X-ray crystallography,[5,11,12] and computational modelling and simulation. An example is the Covid Moonshot initiative, which thanks to the contributions of scientists operating all over the world, has identified several potential M^{pro} inhibitors hits which are now under biochemical evaluation.[13]

The best characterized M^{pro} inhibitors so far act with a covalent mechanism. They share a similar recognition moiety, *i.e.* a peptidomimetic scaffold of moderate size with a glutamine or an isostere at the P1 position and a branched lipophilic group at P2,[5,11,12] and are equipped with a reactive 'warhead', *i.e.* an electrophilic group responsible for the covalent modification of the M^{pro} (see Scheme 1). Warheads so far employed for the design of SARS-CoV-2 inhibitors ranged from classical Michael acceptors (MAs) to activated carbonyl derivatives, including alpha-ketoamides and aldehydes.

For covalent modification of cysteine residues, the MA class is often the first choice with several examples of approved drugs containing this group.[14–17] Despite the potential problem of off–target interactions due to the electrophilicity of α,β unsaturated systems, MAs are widely employed against cysteine proteases because they ensure the covalent inhibition of the enzyme.[18] Compounds equipped with less reactive warheads (*i.e.* carbonyl-based compounds or nitriles) act as reversible inhibitors, as they form metastable adducts (such as hemithioketal or thioimidate species) with cysteine residues. In terms of target engagement, duration of inhibition and efficacy, MAs have important potential advantages over other warheads.[16–18] Previous work on other viral M^{pro}s exemplifies this: peptidyl

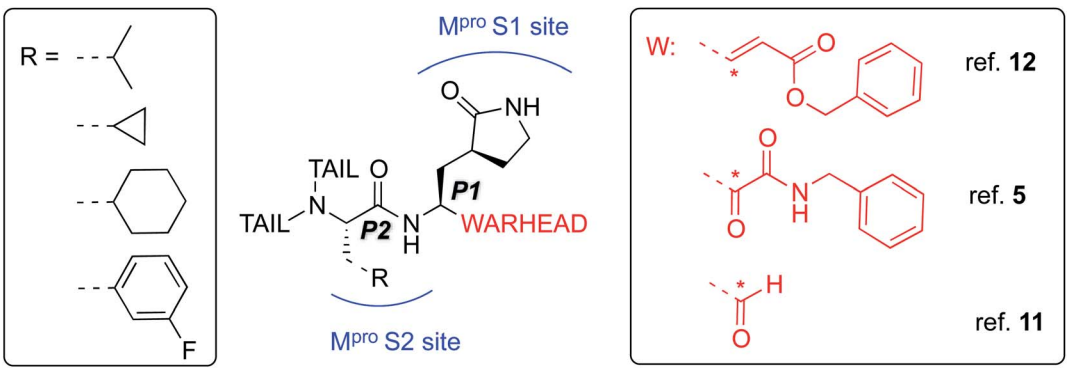

Scheme 1 Schematic representation of the main classes of covalent inhibitors of CoVs M^{pro} so far reported. The reactive center on the warhead is marked with an asterisk. R emerging from P2 residue represents a lipophilic group of moderate size. The tail region is a highly variable portion in term of size and shape and involved other M^{pro} sub-pockets (*i.e.* S3 and S4) not represented in the scheme.

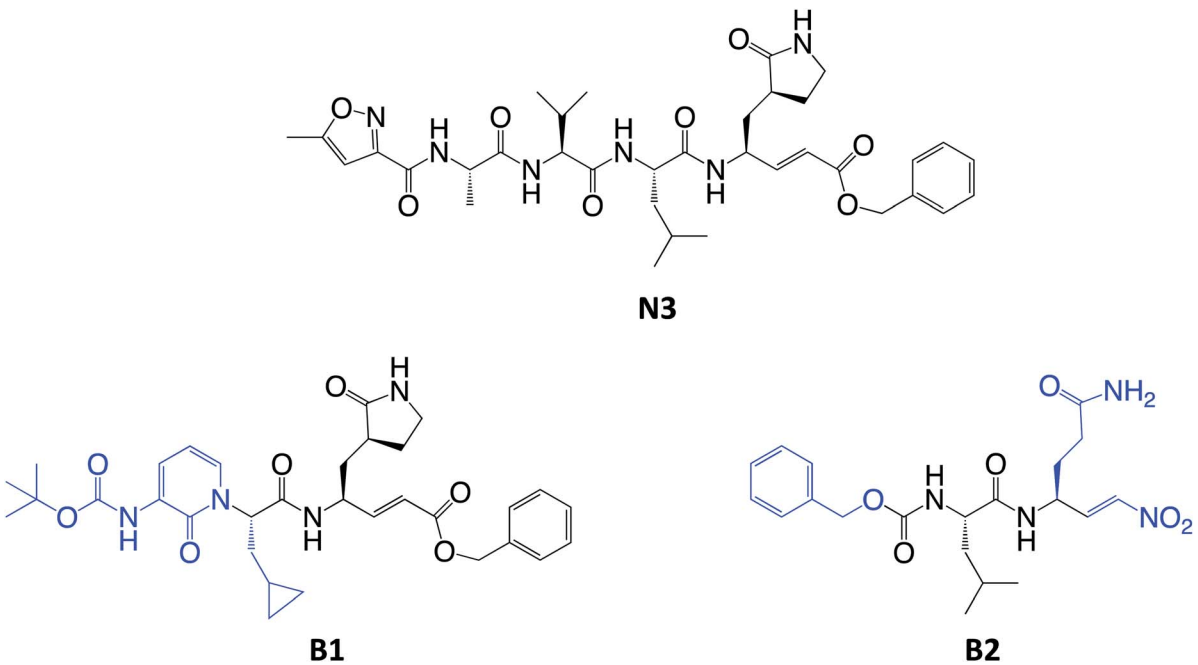

Scheme 2 Chemical structures of known (**N3**) and proposed (**B1** and **B2**) Michael acceptor inhibitors of SARS-CoV-2 M^{pro}. The modifications from **N3** to **B1** and **B2** are highlighted in blue.

MAs were the first class of mechanism-based covalent inhibitors of CoV M^{pro} enzymes described in 2005.[19] This seminal work prompted Jin and colleagues[12] to test this library of compounds on the SARS-CoV-2 M^{pro}. Among those compounds, they found one, **N3** (see Scheme 2), which shows promising inhibitory activity against the M^{pro} of SARS-CoV-2.

Kinetic analysis of the inhibition of M^{pro} of SARS-CoV-2 by **N3** suggests a mechanism of two steps leading to irreversible inactivation (see Scheme 3): protein-inhibitor association to form a noncovalent complex (**E:I**), followed by covalent bond formation (**E-I**).[5] The X-ray diffraction structure indicates a covalent bond between the S atom of Cys145 of protomer A and the Cβ atom of the vinyl group (see Scheme 3), thus confirming that **N3** is a MA inhibitor[12] and confirming that SARS-CoV-2 M^{pro} is a CP with an active site catalytic dyad (C145/H41) similar to other CPs.

Crystallographic electron density maps of **N3** (ref. 12) indicate hydrogen bond and van der Waals interactions between the inhibitor and residues in the substrate-binding pockets of M^{pro}. An exception is the solvent-exposed Val at P3, suggesting that this site can tolerate substituents of different shape and size.[12]

Mechanistically, it is proposed that the chemical reaction leading to M^{pro} inactivation requires the imidazole group of H41 to activate the SH group of C145 to form a highly nucleophilic $CysS^-/HisH^+$ ion pair that would readily react with the inhibitor.[20] This equilibrium may be tipped in favour of the ion pair by ligand binding, and may depend on the features of the ligand itself. In this regard, the inactivation of SARS-CoV-2 M^{pro} by covalent (peptidyl) inhibitors, including **N3**, can be considered as equivalent to the acylation step of the proteolysis reaction in CPs. According to our previous QM/MM study on the proteolysis reaction catalyzed by cruzain CP, the proton from the cationic $HisH^+$ is transferred to the N atom of the scissile peptide bond, followed by Cys attack on the carbonyl carbon atom of the peptide.[21] However, our recent study on the proteolysis reaction of SARS-CoV-2 M^{pro} using as substrate the polypeptide Ac–Val–Lys–Leu–Gln–ACC (ACC being a fluorescent tag 7-amino-4-carbamoylmethylcoumarin) suggests that the mechanism of action of this enzyme differs from most other CPs.[22] First of all, the enzyme:substrate initial complex would correspond to the neutral C145/H41 dyad (equivalent to **E:I** in Scheme 3) instead of the ionic pair dyad $C145^-/H41^+$ ($\mathbf{E^{(+/-)}:I}$ in Scheme 3). From this stable state, the acylation reaction consists of a proton transfer from C145 to the H41 concomitant with the nucleophilic attack on the carbonyl carbon atom of the peptide bond by the sulfur atom of C145, leading to a pseudostable intermediate. Then, the cleavage of the peptide bond by M^{pro} is assisted by proton transfer from the protonated $H41^+$ to the nitrogen atom of the substrate, forming an acyl-enzyme covalent intermediate. This last step of the acylation was calculated to be almost barrierless with the substrate employed in our previous study.[22] In the inhibition reaction by MA compounds shown in Scheme 2, the proton will be transferred from the protonated $H41^+$ to the Cα of the inhibitor, thus leading to the covalent **E-I** adduct (Scheme 3). Consequently, in the design of covalent inhibitors, focus must be put on

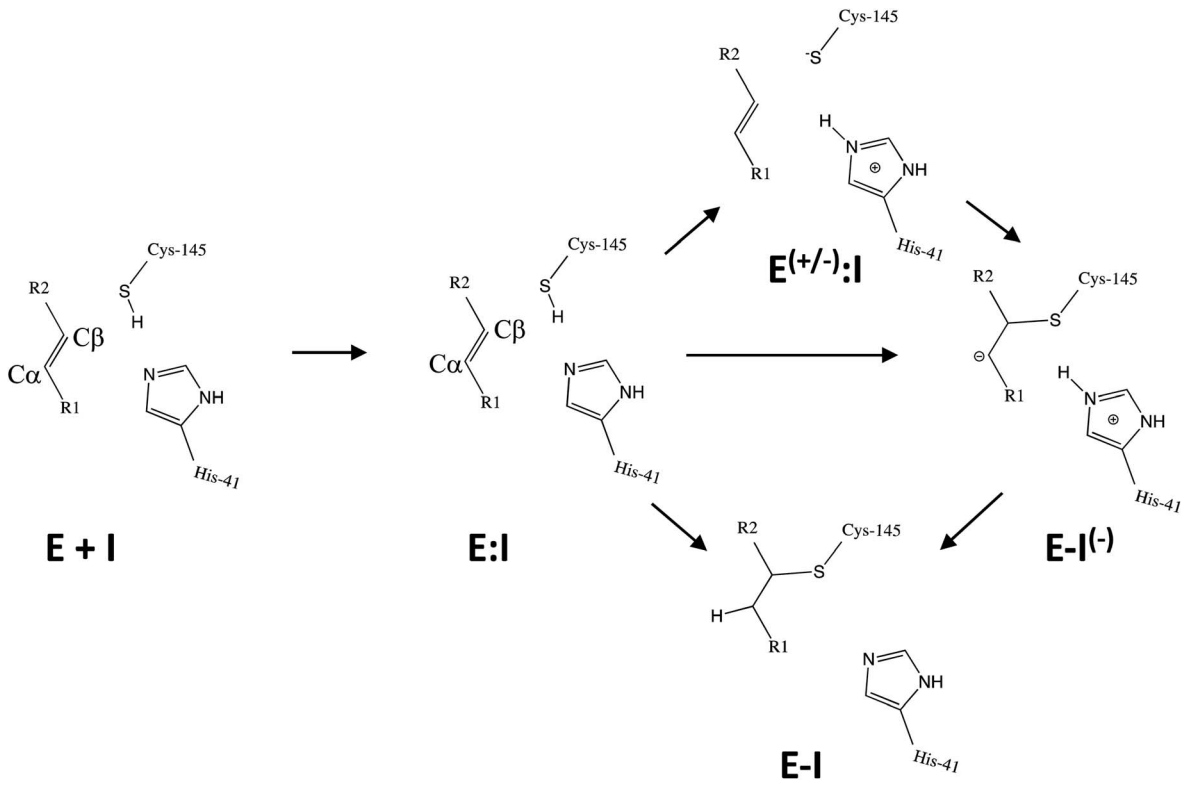

Scheme 3 Possible general mechanisms of SARS-CoV-2 M^{pro} cysteine protease inhibition by Michael acceptor inhibitors: concerted or stepwise Michael addition. R1 and R2 represent different substituents, as shown in compounds depicted in Scheme 2.

obtaining an exergonic process for the **E-I** formation, with low activation energy barriers. The energy barriers from **E-I** back to reactants **E:I** will determine the irreversible *vs.* reversible character of the inhibitors, with potentially paramount importance for finding the optimal balance between efficacy and safety.[23] To reach this goal, in addition to the presence of a reactive warhead, the interactions between the recognition moiety of the inhibitor and the different sub-sites of the binding pocket of the protein must be taken into account.[17] Design can be guided by the results derived from previous studies on this and related CPs. QM/MM simulations provide a good tool to investigate the reactivity of covalent inhibitors within their protein targets.[24–30]

Here, we focus firstly on the inhibition of the SARS-CoV-2 M^{pro} by the covalent (peptidyl) irreversible inhibitor **N3**, modelling the reaction with QM/MM techniques. Building upon these findings, on information derived from other CP inhibitors, and on our previous study on the proteolysis reaction of M^{pro},[22] we then designed, and tested computationally, two MA inhibitors to block the enzyme: compounds **B1** and **B2** in Scheme 2. **B1** was designed according to some of the modifications made by Zhang *et al.*[5] on their broad-spectrum peptidomimetic α-ketoamides inhibiting of the main proteases of betacoronaviruses, alphacoronaviruses and the 3C proteases of enteroviruses.[31] In addition, although the inhibition of CPs has been proposed to depend on interactions between the peptidic framework (the P2) of the inhibitor and the S2 pocket of the enzyme,[29,32–35] this is probably not the case in SARS-CoV-2 M^{pro}, according to the QM-MM protein-substrate interactions found in our previous study of the proteolysis reaction:[22] S2 appears to be a small hydrophobic pocket without strong hydrogen bond interactions. Therefore, the isopropyl group of Leu at P2 site was replaced by a cyclopropyl group. This change is in accordance with the changes by Zhang *et al.* to the original peptidomimetic α-ketoamides to enhance anti-viral activity against beta coronaviruses (such as SARS-CoV and SARS-CoV-2).[5] The tail of the **N3** compound was replaced by an amino pyridone moiety carbamoylated by a *tert*-butyloxycarbonyl group, because this group is expected not to be a substrate of cellular proteases, and so offers potential advantages in term of pharmacokinetic properties.[5] Our previous M^{pro} proteolysis reaction study indicated that the S3 subsite is completely exposed to the solvent; only three interactions between the peptide backbone atoms of Lys3 of the substrate and the protein were observed.[22] In addition, the lack of strong hydrogen bond interactions in the S4 sub-site supports the strategy of reducing the size of the inhibitor.

In the case of compound **B2**, a more dramatic modification was introduced: we decided to change the warhead to a nitroalkene, based on the potent reversible inhibitory activity of a family of dipeptidyl nitroalkene derivatives against the CPs cruzain and rhodesain by one of us,[14] together with our previous QM/MM study on the inhibition mechanism of three CPs belonging to the papain family (cruzain, rhodesain, and cathepsin L).[29] Based upon the mechanism depicted in Scheme 3, the protonation of intermediate $\mathbf{E\text{-}I}^{(-)}$ might be less favored in the case of the nitroalkane carbanion because the acidity of the corresponding acid, namely the nitroalkane, is higher, and thus, the basicity of the carbanion is lower; potentially being a reversible covalent inhibitor. The glutamine residue in P1 was introduced due to the strong favorable interactions that we observed in the study of the proteolysis of the Ac–Val–Lys–Leu–Gln–ACC substrate by M^{pro},[22] and based on the substrate specificity of SARS-CoV M^{pro}, *i.e.* requiring glutamine in the P1 position.[36] P2 was kept the same as in **N3**, while the rest of the inhibitor in positions P3, P4 and P5 was replaced by a smaller moiety, with the aim of improving the physicochemical properties as well as synthetic accessibility. Importantly, both designed compounds **B1** and **B2** should be readily prepared through synthetic approaches inspired by published synthetic routes of similar compounds.[13,37]

Methods

The atomic coordinates of SARS-CoV-2 M^{pro} were taken from the X-ray structure of its complex with the **N3** inhibitor, available in the Protein Data Bank (PDB ID 6LU7).[12] The biological assembly (homodimer) was built using Discovery Studio Visualizer 19. Inhibitor **N3** was replaced by two Michael acceptor inhibitors (compounds **B1** and **B2**) to create two new covalent enzyme-inhibitor models (**E-I** in Scheme 2). Once the enzyme-inhibitor models were set up, solvated with a box of water molecules and equilibrated by means of preliminary MM molecular dynamics (MD) simulations (Fig. S1a, S2a and S3a†), QM/MM free energy surfaces (FESs) were calculated, in terms of Potentials of Mean Force (PMFs), for every step of the reaction, using umbrella sampling[38] combined with the Weighted Histogram Analysis Method (WHAM)[39] see ESI† for details. The QM region consisted of 75 atoms for the inhibitor **N3** and compound **B1**, and 57 atoms for the compound **B2** including P1′, P1 and P2 fragments of the inhibitors and the two catalytic residues C145 and H41. Four quantum 'link' atoms were inserted where the QM-MM frontier crosses a covalent bond (see Fig. S1b, S2b and S3b†), as in our study on proteolysis of SARS-CoV-2 M^{pro} enzyme.[22] The Austin Model 1 (AM1)[40] semiempirical method was used to treat the QM region in the initial exploration of the FESs. The Minnesota Density Functional M06-2X[41] (with the standard 6-31+G(d,p) basis set[42]) as implemented in the Gaussian09 program,[43] was used to treat the QM region, to calculate the final corrected high level FESs (see ESI† for details), as well as for the geometry optimizations of the different transition states. This is a good choice of functional and basis set, based on our previous tests and experience,[44–46] including the study of the proteolysis reaction of SARS-CoV-2 M^{pro}.[22] The protein and water molecules were treated with the AMBER ff03 (ref. 47) and TIP3P[48] force fields, respectively. QM/MM MD simulations were performed using the fDynamo library,[49] using procedures that we have previously extensively tested and validated. Structures of all the important states involved in the reaction (minima and transition state structures) were then optimized at the M06-2X:6-31+G(d,p)/MM level, starting from representative AM1/MM snapshots from the FESs, with Gaussian09 (ref. 43) coupled to the fDynamo library. The corrected free energy surfaces are designated M06-2X/6-31+G(d,p):AM1/MM. These structures are deposited in the ESI.†

The inhibitor:M^{pro} binding energy was estimated by docking calculations for **N3**, **B1** and **B2**, with the Glide program,[50] starting from the QM/MM structures of the enzyme:inhibitor non-covalent reactant complex, **E:I** in Scheme 2 (see ESI† for details).

Results and discussion

Inhibition reaction of SARS-CoV-2 M^{pro} with N3

The first step of our program towards the design of new SARS-CoV M^{pro} inhibitors was the study of the reaction with the **N3** inhibitor originally proposed by Yang *et al.*[19] As described in the Methods section, the enzyme-inhibitor covalent **E-I** complex was equilibrated by MM and QM/MM MD simulations. A schematic representation of the equilibrated structure of the active site is shown in Fig. 1, where important interactions found in the MD simulations and the X-ray structure obtained by Jin *et al.*[12] are indicated as blue and red dashed lines, respectively. The pattern of interactions between the enzyme and the inhibitor in our equilibrated structure is quite close to that observed crystallographically, thus supporting our starting structure for the exploration of the full mechanism. The MD results confirm the absence of hydrogen bond interactions with some of the side chains of the residues of **N3** (P2–P5) which, considering the demonstrated efficiency of this inhibitor, can be used as a guide for the design of improved compounds not requiring hydrogen bond interactions with these sites, as mentioned in the Introduction.

Once the covalent enzyme-inhibitor **E-I** complex was equilibrated, the Michael addition reaction and the proton transfer from the protonated H41 to the Cα atom of the inhibitor (see Scheme 3) was explored backwards from **E-I** to **E:I** by QM/MM MD simulations. Appropriate combinations of interatomic distances were employed to generate the potential energy surfaces (PESs) and the free energy surfaces (FESs) of every chemical step. These reaction coordinates were chosen based on previous experience and testing for this and similar reactions (see ESI† for details, including convergence tests). The FESs obtained (see Fig. S7 in ESI†) show that the most stable protonation state of the C145/H41 dyad corresponds to that in which both residues are neutral, designated **E:I**. This result is in contrast with previous computational studies of proteolysis[21] and inhibition[25,29,51] and earlier suggestions for other SARS-CoV main proteases that inhibitor binding may favor formation of the ion pair,[52] but it is in agreement with our previous study of the proteolysis reaction of M^{pro}.[22] From this initial state, the proton transfer from C145 to H41 to form the ionic dyad $\mathbf{E^{(+/-)}}$**:I** precedes the Michael addition that forms the covalent bond between the sulphur atom of C145 and the Cβ of the inhibitor, to form $\mathbf{E:I^{(-)}}$. Finally, the proton transfer from His41 to Cα of the substrate takes place as an almost barrierless process to produce the final, stable, **E-I** covalent complex. The resulting free energy profile is shown in Fig. 2, and details of the active site in the key states in the inhibition process are presented in Fig. 3. The reaction is a stepwise process, kinetically controlled by the carbon–sulphur bond formation, *via* **TS2**, with a free energy barrier of 11.2 kcal·mol^{-1}, and a reaction energy of −17.9 kcal mol^{-1}. The low activation free energy of the inhibition reaction with **N3** is in agreement with the experiments that revealed a process so fast that the enzyme inactivation-rate constant for covalent bond formation could not be measured.[12] Regarding the thermodynamics, the resulting energy profile is in agreement with the irreversible character of the inhibition considering that activation barrier for the reverse retro-Michael reaction is nearly 30 kcal mol^{-1} (computed as the difference between **E-I** and **TS2**). On the other side, the free energy of activation for the initial proton transfer from C145 to H41 is very low (1.4 kcal mol^{-1}) and the relative energy of the ion pair dyad, $\mathbf{E^{(+/-)}}$**:I**, is only 1.3 kcal mol^{-1} higher than the starting **E:I** state

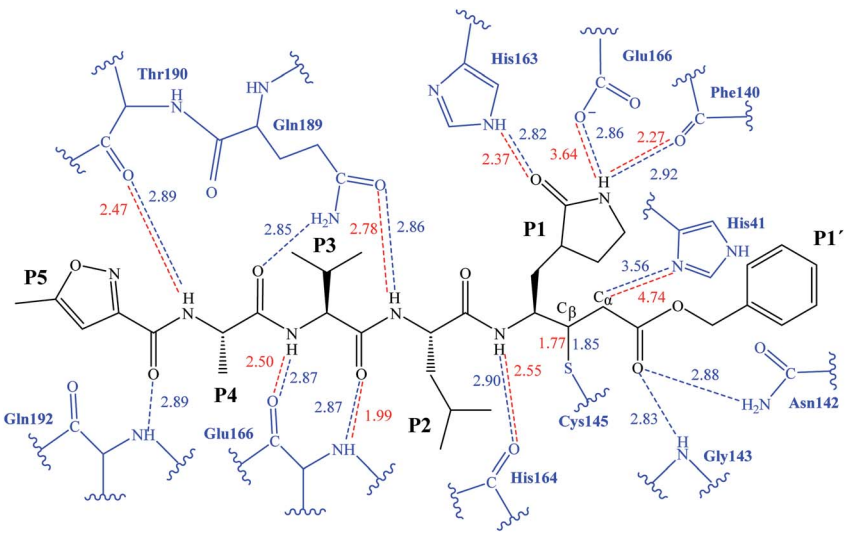

Fig. 1 Schematic representation of **N3** in the covalent **E-I** complex in the active site of SARS-CoV-2 M^{pro}. The dashed lines indicate hydrogen bond interactions between the inhibitor the protein found in MD simulations (blue lines) and the X-ray structure (red lines) obtained by Jin *et al.*[12] Interatomic distances, computed as average values over the MD simulations (in blue) and from the X-ray structure (in red), are reported in Å.

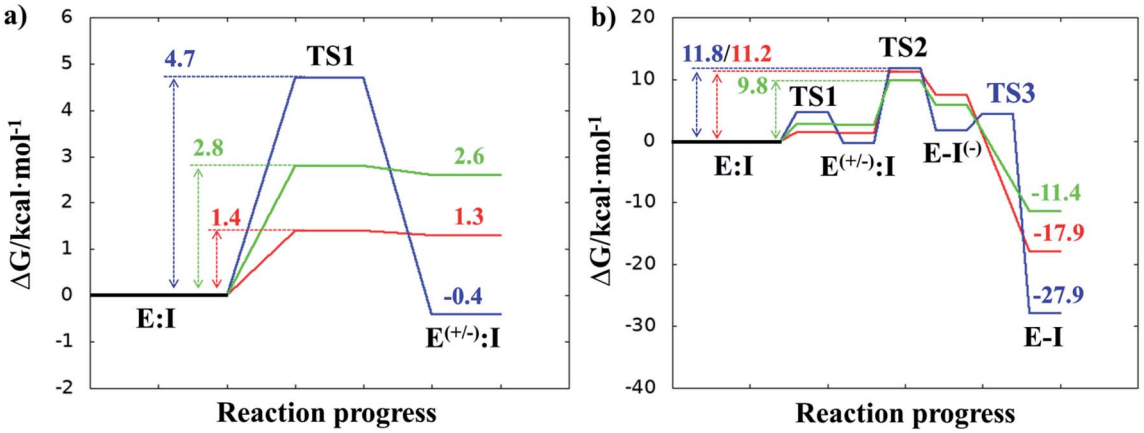

Fig. 2 M06-2X/6-31+G(d,p):AM1/MM free energy profiles for covalent complex formation with SARS-CoV-2 M^{pro} and: **N3** (red line); compound **B1** (blue line); and compound **B2** (green line). Panel (a) shows the formation of the ion pair $E^{(+/-)}$:I; and the full inhibition reaction is shown in panel (b). Energies are in kcal·mol^{-1}.

(see red line in Fig. 2a). It is important to point out that while preparing the present manuscript, a QM/MM MD study on the mechanism of **N3** appeared, where a different DFT Hamiltonian (B3LYP) was used to describe the QM region, as well as a different sampling method.[53] Comparison of the two studies reveals some analogies but also some important differences. The stepwise and the exergonic character of the reaction, and the finding that the neutral **E:I** form is more stable than the ion pair $E^{(+/-)}$:**I**, are common to both studies. However, while our $E^{(+/-)}$:**I** is just 1.3 kcal mol^{-1} higher in energy than **E:I**, the difference obtained in the ref. 53 is much higher (10.3 kcal mol^{-1}). Similarly, those workers found a much higher energy barrier for the C145–Cβ bond formation from **E:I** (20.9 kcal·mol^{-1}). These differences may arise because of the different level of QM theory used. The mechanism is also slightly different because a water molecule is used in the transfer of the proton from His41 to Cα of the inhibitor while, as commented above, our simulations show that the direct transfer can take place, in an almost barrierless process, as previously for other CP inhibition reactions by Michael acceptors.[29,51] We note that, all other things being equal, the lower barrier found here (not involving an intervening water molecule), indicates that the mechanism we find would dominate the experimentally observed kinetics.

Structural analysis of the structures of the states in the reaction (Fig. 3, Tables S5 and S6†) confirms the mechanism and suggests that the active site of the M^{pro} does not undergo dramatic changes during the chemical steps. The two catalytic residues are well oriented in the reactive non-covalent complex **E:I** in which the inhibitor is well anchored to the active site. Structures of **TS1** and **TS2** were optimized at the M06-2X/6-31+G(d,p)/MM level and the minimum energy path, computed as the IRC path, confirms the predictions derived from the M06-2X:AM1/MM FESs (see Tables S5–S7†).

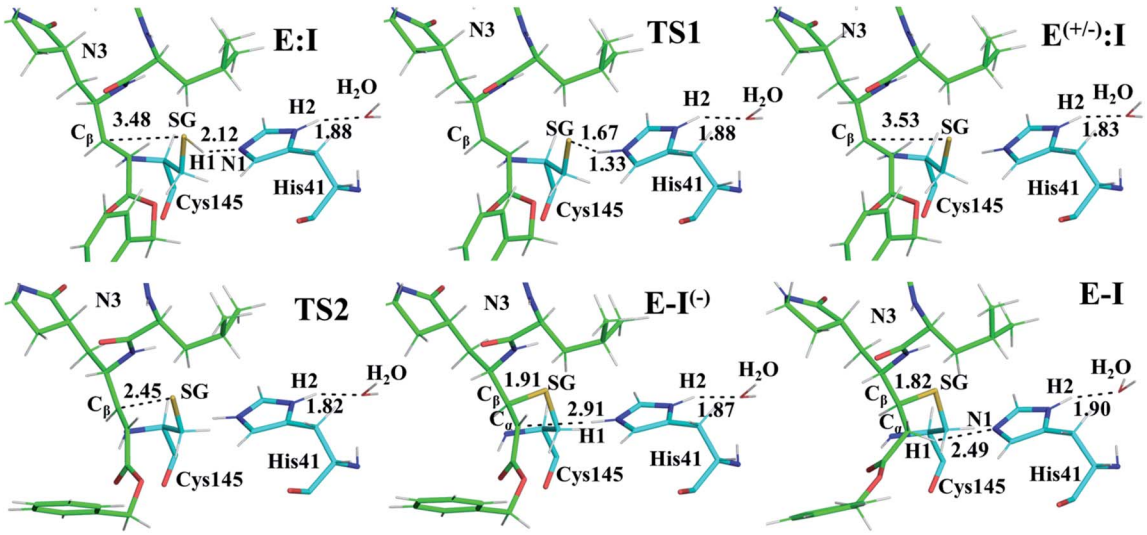

Fig. 3 Detail of the M06-2X/6-31+G(d,p)/MM optimized structures of the important states in the inhibition process of M^{pro} by **N3**. Carbon atoms of the inhibitor are shown in green while those of the catalytic residues Cys145 and His41 are in blue. Key distances are in Å.

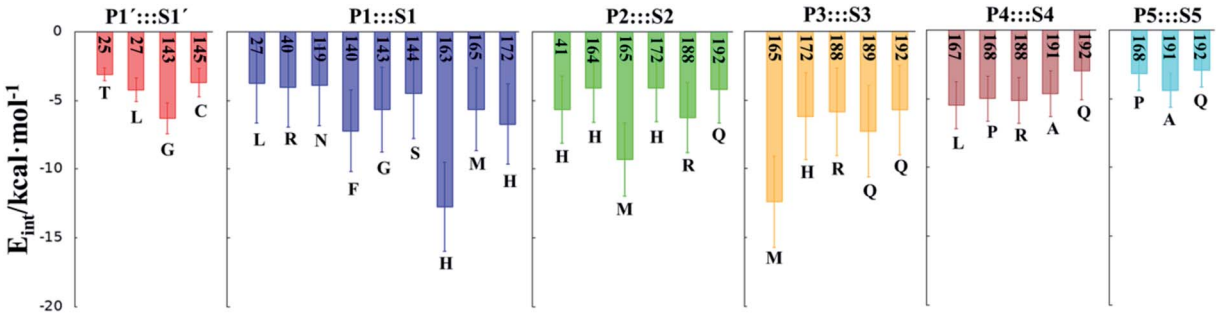

Fig. 4 Main favorable average interaction energies (electrostatic plus Lennard-Jones) between residues of Chain-A and each fragment of the **N3** computed in the **E:I** state. Results obtained as an average over 1000 structures of the AM1/MM MD simulations.

In order to analyse the non-covalent enzyme:inhibitor reactant complexes, **E:I**, the interaction energies (electrostatic plus Lennard-Jones) between residues of Chain-A of M^{pro} and each fragment of the **N3** were computed as an average over 1000 structures of the equilibration AM1/MM MD simulation (Fig. 4). The pattern of interactions is similar to that of **E-I**, shown in Fig. 1, confirming that the inhibitor and enzyme undergo no large structural changes during the chemical steps of the inhibition process. It is important to point out that, while there are protein residues that clearly bind the inhibitor in the active site, which could have been predicted by the X-ray geometrical analysis of the **E–I** complex (N142 and G143 in P1′ ::: S1′, H163, E166, F140 and H164 in P1 ::: S1, Q189 in P2 ::: S2, E166 in P3 ::: S3, T190 in P4 ::: S4 or Q192 in P5 ::: S5), some of these residues do not form binding interactions in **E:I**. For instance, interatomic distances (Table S5†), suggest that E166 forms a hydrogen bond with the backbone of P3, but no net stabilizing interaction was found (Fig. 4 and S8†) in **E:I**. Therefore, design of **N3** analogues to generate a more stable enzyme-inhibitor initial complex should not be limited to geometrical analysis of X-ray structures or those derived from MD simulations of the reactant complex. Overall, our results suggest that P1 is the most important fragment to consider in the design of new efficient inhibitors. This accords with the conclusions of our QM/MM study of the proteolysis reaction of M^{pro}.[22]

Designed inhibitors of SARS-CoV-2 M^{pro}: compounds B1 and B2

After the study of the Michael addition with inhibitor **N3**, the inhibition reactions of M^{pro} with compounds **B1** and **B2** were simulated using the same methods. The calculations analyzed the stability of the **E-I** complexes, with special attention to the protein-inhibitor interactions. A schematic representation of the equilibrated **E-I** structures of the active site after the QM/MM MD simulation is shown in Fig. 5. The interactions between the enzyme and the two proposed inhibitors, indicated as dashed blue lines in Fig. 5, confirm the predictions of the design. In both cases, the interactions between the protein and the inhibitor are dominated by the P1′:::S1′ and the P1:::S1. Apart from these interactions, in the case of compound **B1**, hydrogen bond interactions in P4 (with Gln192) are found, while in the case of compound **B2** more strong interactions appear, especially in P3 (with Glu166). These interactions keep

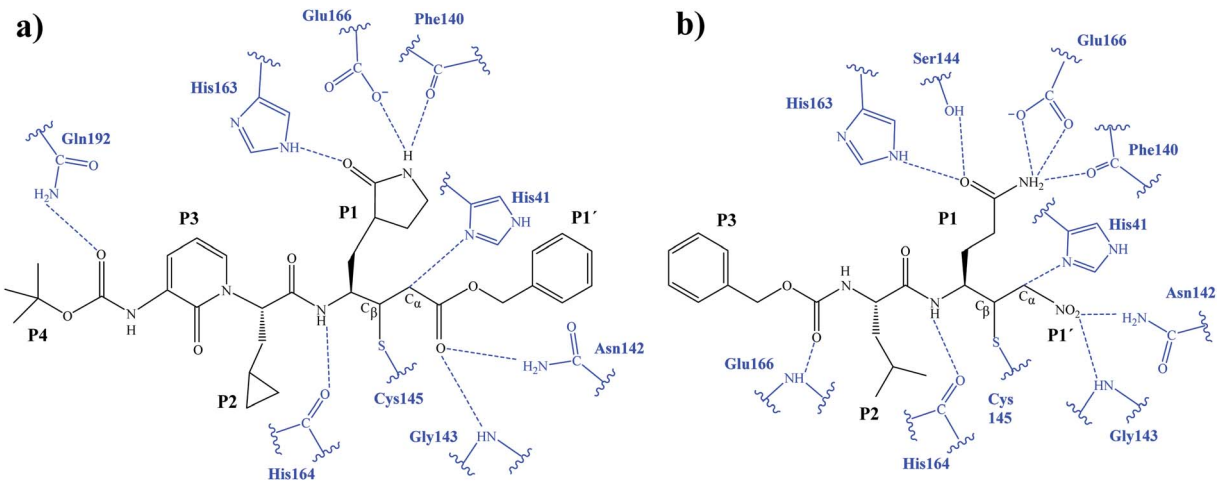

Fig. 5 Schematic representation of the active site in the **E-I** complex and details of the H-bond interactions between the inhibitor and the active site of the SARS-CoV-2 M^{pro} from QM/MM MD simulations of compound **B1** (a) and compound **B2** (b).

both compounds posed appropriately for covalent bond formation to take place.

After equilibration of the two covalent **E-I** structures, the chemical reaction steps of the (reverse) inhibition process were studied by exploration of the PESs and FESs (Fig. S9 and S11†). The free energy profiles are shown in Fig. 2, together with that for **N3**. The reaction in both cases follows the same mechanism as for **N3**. The activation energy barriers obtained with compound **B1** and **B2**, are both determined by the rate-limiting transition state of the C–S bond formation, **TS2**. Nevertheless, while the barrier (for covalent complex formation, *i.e.* for the forward reaction) of **B1** (11.8 kcal mol^{-1}) is very close to that obtained with **N3** (11.2 kcal mol^{-1}), that of **B2** is slightly lower (9.8 kcal mol^{-1}). In contrast, the reaction energies of **B1** and **B2** are very different: −27.9 and −11.4 kcal mol^{-1}, respectively. These results suggest, first, that both designed inhibitors should present similar reactivity to **N3** for covalent complex formation, with **B2** being slightly more reactive. Second, while compound **B1** would be an irreversible inhibitor, compound **B2** is predicted to show more reversible inhibitor character than **B1** and **N3**. As can be seen from Fig. 2a, there are also differences regarding the relative energy of the initial non-covalent states, **E:I** *vs.* **E$^{(+/-)}$:I**. While in the case of compound **B1** the neutral dyad is 0.4 kcal·mol^{-1} less stable than the ionic pair, the **E$^{(+/-)}$:I** of compound **B2** is 2.6 kcal mol^{-1} higher in energy than the **E:I**. As observed in Fig. 2a, **E$^{(+/-)}$:I** of compound **N3** is also higher in energy, by 1.3 kcal mol^{-1}, than the **E:I**. These results, consistent with the results obtained with **N3**, with the previously studied proteolysis reaction with a reactive substrate,[22] and with previous studied on other SARS-CoV M^{pro} enzymes[52] indicate that the protonation state of C145 and H41 in the initial non-covalent binary complex depends on the substrate substituents in the P1′, P1 and P2 positions. It is remarkable how, according to the P1′⋯S1′ interatomic distances, the interaction between the nitro group of **B2** and G143 appears to be stronger in the **E:I** than in **E$^{(+/-)}$:I**, in contrast to **B1**, which shows a only small decrease in the distances between the carbonyl group and residues G143; **N3** that does not show any clear change in the interactions with residues G143, S144 and C145 (see Tables S5, S8 and S11†). The different electronic distributions in these molecules (a less basic carbanion in **B2** as compared to **N3** and **B1**) may slightly shift the pKa of the two catalytic residues. Nevertheless, as shown in Fig. 2, this influence is not significant for the inhibition process of M^{pro}. Finally, while the final proton transfer from H41 to the Cα of the inhibitor takes place as a barrierless process in **N3** and **B2**, a transition state, **TS3**, is found for the reaction with **B1**, with a very small energy barrier (2.7 kcal mol^{-1}).

M06-2X/6-31+G(d,p)/MM optimized structures of the stable states in the reactions with both inhibitors are presented in Fig. 6 (structures of the TSs, **E:I** and **E-I** are given in the ESI,† together with a list of key interatomic distances of average structures obtained from the AM1/MM MD simulations and single optimized structures at the M06-2X/6-31+G(d,p)/MM level). As observed for **N3**, the enzyme-inhibitor interactions do not change significantly during the inhibition reaction with **B1** and **B2** (Fig. 6, Tables S8 and S11†). In both cases, designed inhibitors bind stably in the active site of the enzyme. Analysis of the favorable protein-inhibitor interactions in the **E:I** state, computed as the sum of QM/MM electrostatic and Lennard-Jones terms, shown in Fig. 7, confirms the predictions made in the design of **B1** and **B2** and the conclusions from the geometrical analysis of the optimized structures. In both cases the interactions between the protein and the inhibitors are dominated by those in the P1⋯S1 site.

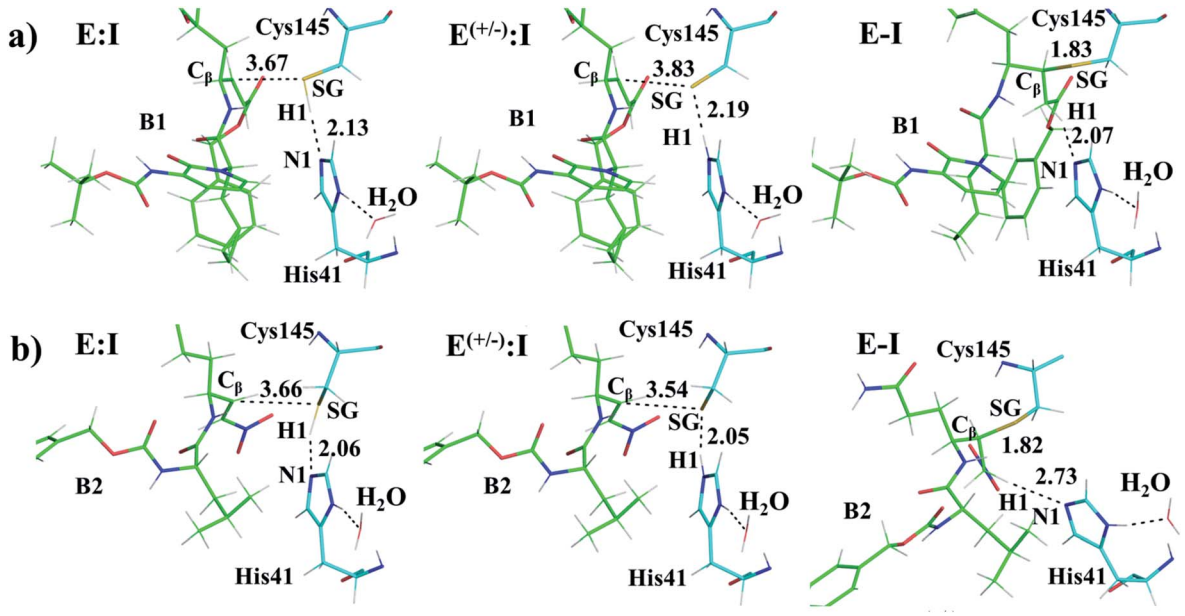

Fig. 6 Detail of the M06-2X/6-31+G(d,p)/MM optimized structures of E:I, E$^{(+/-)}$:I and E-I appearing along the inhibition process of M^{pro} by compound B1 (a) and compound B2 (b). Carbon atoms of the inhibitors are shown in green while those of the catalytic residues Cys145 and His41 are in blue. Key distances are in Å.

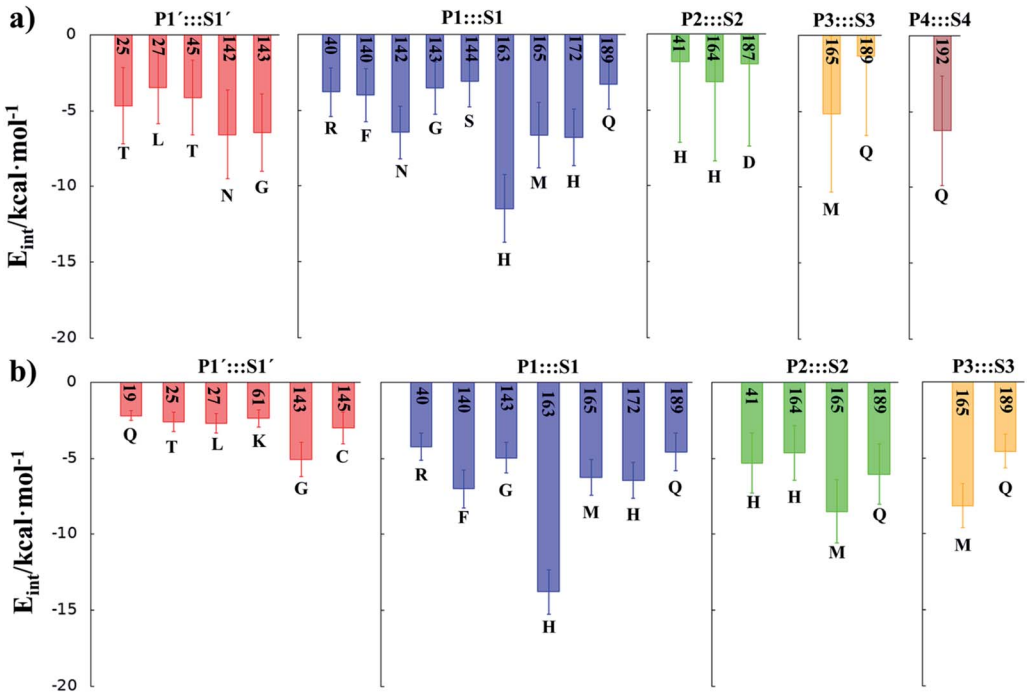

Fig. 7 Main favorable average interaction energies (electrostatic plus Lennard-Jones) between residues of Chain-A and each fragment of the compound **B1** (a) and compound **B2** (b) computed in the **E:I** state. Results obtained as an average over 1000 structures from the AM1/MM MD simulations.

The averaged structures of **E:I** and **TS2** in the three compounds (Tables S5, S8 and S11†), from the QM/MM MD simulations, show how the smaller the reduction in the distance between the SG atom of C145 and the Cβ atom of the inhibitors (the reaction coordinate that controls the rate-limiting step) from **E:I** complex to the **TS2** (1.11, 1.09 and 0.74 Å for **B1**, **N3**, and **B2**, respectively), the lower the barrier (11.8, 11.2 and 9.8 kcal mol^{-1} for **B1**, **N3** and **B2**, respectively). These results suggest that **B2** adopts a more reactive conformation in the **E:I** state, closer to **TS2** than those of **N3** or **B1**, which may contribute to its lower overall activation energy barrier. These results explain why the inhibitor in which the ion pair is most disfavored, but structurally closer to the rate-limiting **TS2**, also has the lowest barrier.

Binding poses for designed inhibitors B1 and B2

Binding of inhibitors to the M^{pro} active site through non-covalent interactions (to form **E:I**, Scheme 3) is a key event that precedes the chemical step of the inhibitory process. The ability of **B1** and **B2** to fit the M^{pro} active site was therefore examined, starting from the structures of the reactants generated by QM/MM MD simulations. N3 was used as a control. The best docking pose for each ligand (see Methods) indicates that all the inhibitors assume a binding pose consistent with the X-ray structure of the M^{pro}-**N3** adduct, *i.e.* with the warhead properly oriented to react with the catalytic cysteine, the polar sidechain at P1 site forming hydrogen bonds with S1 residues, and the lipophilic chain at P2 site undertaking several van der Waals contacts with S2 residues (Fig. S13†). Crucially, the binding poses of **B1** and **B2** resemble that of the reference inhibitor **N3** (Fig. S13†), suggesting that modifications at level of the tail or of the warhead do not affect the accommodation of the critical P1 and P2 residues. Within the known limits of empirical scoring functions, the present docking analysis supports the proposal that **B1** and **B2** can bind to M^{pro} in a productive orientation in its active site.

Conclusions

Here, we first explored the inhibition of SARS-CoV-2 M^{pro} with a known covalent (peptidyl) inhibitor, **N3**,[19] by QM/MM MD simulations. The results are in good agreement with experimental crystal structures and kinetics, and reveal the chemical mechanism of covalent reaction. This provides an atomically detailed description of the process of formation of the covalent enzyme-inhibitor complex. We used these results, together with information from other CP protease inhibitors and from our recent study of the proteolysis reaction of SARS-CoV-2 M^{pro},[22] to design and computationally test two putative inhibitors of SARS-CoV-2 M^{pro} based on the scaffold of **N3**. In the first designed compound, **B1**, the recognition portion of **N3** was modified while both the recognition part and the warhead of **N3** (to a nitroalkene) were changed to generate a second compound, **B2** (Scheme 2).

The calculated free energy landscape for formation of the covalent enzyme-inhibitor intermediate indicate that the reaction, with all three compounds, proceeds in a stepwise manner: in the first step, Cys145 is activated by His41, forming the ion

pair $E^{(+/-)}$:**I**, followed in the second step by attack of the sulfur atom of Cys145 on the Cβ atom of the inhibitor and proton transfer from His41 to the Cα atom of the inhibitor, leading a stable covalent **E-I** intermediate. The rate-limiting step of the process, in all three cases, corresponds to the enzyme-inhibitor covalent bond formation, with an activation free energy of 11.2, 11.8 and 9.8 kcal mol^{-1} for **N3**, **B1** and **B2**, respectively. The low activation free energy of the inhibition reaction with **N3** is consistent with kinetic experiments,[12] while the values obtained with compound **B1** and **B2**, indicate that both are also reactive. Further, the lower activation energy for **B2** suggests that it would react faster with M^{pro}: this is a potential advantage in biological media in which the compounds have to compete with high concentration of the natural substrate. Within cells, covalent inhibitors must react with the target quickly, to avoid competing reactions with free bio-nucleophiles, such as glutathione, or with proteases (*e.g.* in the case of peptidyl compounds) that can reduce their active concentrations.[54] From the thermodynamic point of view, the exergonic reaction with **N3** (reaction energy −17.9 kcal mol^{-1}) is consistent with its experimentally observed stability (*e.g.* revealed by X-ray crystallographic structures).[12] The inhibition reactions of M^{pro} with **B1** and **B2** are also exergonic but are very different from each other (−27.9 and −11.4 kcal mol^{-1}, respectively), suggesting that compound **B1** would be an irreversible inhibitor, but compound **B2** has a more reversible character. Analysis of the QM-MM interaction energies between the different residues of the inhibitor and the residues located in the substrate-binding pockets of M^{pro} confirms the predictions made in the design of **B1** and **B2**, and the conclusions from geometrical analysis of the structures optimized at the DFT/MM level. In both cases, the interactions between the protein and the inhibitors are dominated by those in the P1::S1 site. Finally, docking carried out with the noncovalent enzyme:inhibitor reactant complex structures from our QM/MM structures support the proposal that **B1** and **B2** can bind M^{pro} in a reactive conformation in its active site.

In summary, our QM/MM study of the inhibition of M^{pro} by **N3** and two covalent (peptidyl) MA compounds, **B1** and **B2**, which we designed based on these simulations and medicinal chemistry experience, indicates that a lower alkylation barrier than **N3** can be obtained by modulating either the recognition portion or the warhead. Interactions between the recognition moiety and M^{pro} active site affect the chemical step because they dictate the pose of the inhibitor in the active site of the enzyme. Our results show that **B1** has a more irreversible character than **N3** while **B2** is more reversible. This different behavior *in silico* suggest that both compounds should be tested and compared to **N3** as promising candidates as drug leads against COVID-19. Both designed compounds can be easily prepared through synthetic approaches inspired by published synthetic routes of similar compounds.[14,37]

Author contributions

The study was designed by K. Ś., V. M., A. L. and A. J. M. The results were discussed and analyzed by all authors, and contributed to writing the manuscript. K. A., N. S. and K. Ś. carried out the QM/MM calculations. A. L. carried out the docking calculations. All authors contributed to discussion and design of inhibitors. All authors have given approval to the final version of the manuscript.

Conflicts of interest

There are no conflicts to declare.

Acknowledgements

This work was supported by the Spanish Ministerio de Ciencia, Innovación y Universidades (Grant PGC2018-094852-B-C21 and PID2019-107098RJ-I00), Generalitat Valenciana (Grant AICO/2019/195 and SEJI/2020/007) Universitat Jaume I (UJI B2017-31, UJI B2018-41, UJI-A2019-04 and SomUJIContraCovid crowdfunding campaign), KŚ thanks the Spanish Ministerio de Ciencia, Innovación y Universidades for a Juan de la Cierva – Incorporación (ref. IJCI-2016-27503) contract. K. A. thanks Universitat Jaume I (POSDOC-A/2018/30) and Generalitat Valenciana (APOSTD/2020/015) for post-doctoral contracts. NS thanks the MINECO for doctoral FPI grant (BES-2016-078029). The authors thankfully acknowledge the computer resources at Pirineus and the technical support provided at Pirineus and by Barcelona Supercomputing Center (QSB-2020-2-0004), as well as the local computational resources of the Servei d'Informàtica of Universitat Jaume I. AJM thanks EPSRC for support (CCP-BioSim, grant number EP/M022609/1) and also the British Society for Antimicrobial Chemotherapy (grant number BSAC-COVID-30).

References

1 G. Zhu, C. Zhu, Y. Zhu and F. Sun, *Current Research in Microbial Sciences*, 2020, **1**, 53–61.
2 A. K. Ghosh, M. Brindisi, D. Shahabi, M. E. Chapman and A. D. Mesecar, *ChemMedChem*, 2020, **15**, 907–932.
3 R. T. Eastman, J. S. Roth, K. R. Brimacombe, A. Simeonov, M. Shen, S. Patnaik and M. D. Hall, *ACS Central Science*, 2020, **6**, 672–683.
4 T. Warren, R. Jordan, M. Lo, V. Soloveva, A. Ray, R. Bannister, R. Mackman, M. Perron, K. Stray, J. Feng, Y. Xu, J. Wells, K. Stuthman, L. Welch, E. Doerffler, L. Zhang, K. Chun, H. Hui, S. Neville, W. Lew, Y. Park, D. Babusis, R. Strickley, P. Wong, S. Swaminathan, W. Lee, D. Mayers, T. Cihlar and S. Bavari, *Open Forum Infect. Dis.*, 2015, **2**, LB-2.
5 L. Zhang, D. Lin, X. Sun, U. Curth, C. Drosten, L. Sauerhering, S. Becker, K. Rox and R. Hilgenfeld, *Science*, 2020, **368**, 409–412.
6 J. H. Beigel, K. M. Tomashek, L. E. Dodd, A. K. Mehta, B. S. Zingman, A. C. Kalil, E. Hohmann, H. Y. Chu, A. Luetkemeyer, S. Kline, D. Lopez de Castilla, R. W. Finberg, K. Dierberg, V. Tapson, L. Hsieh, T. F. Patterson, R. Paredes, D. A. Sweeney, W. R. Short, G. Touloumi, D. C. Lye, N. Ohmagari, M.-d. Oh, G. M. Ruiz-Palacios, T. Benfield, G. Fätkenheuer,

M. G. Kortepeter, R. L. Atmar, C. B. Creech, J. Lundgren, A. G. Babiker, S. Pett, J. D. Neaton, T. H. Burgess, T. Bonnett, M. Green, M. Makowski, A. Osinusi, S. Nayak and H. C. Lane, *N. Engl. J. Med.*, 2020, **383**, 1813–1826.

7 L. Lisi, P. M. Lacal, M. L. Barbaccia and G. Graziani, *Biochem. Pharmacol.*, 2020, 114169, DOI: 10.1016/j.bcp.2020.114169.

8 J. D. Norrie, *Lancet*, 2020, **395**, 1525–1527.

9 L. Riva, S. Yuan, X. Yin, L. Martin-Sancho, N. Matsunaga, L. Pache, S. Burgstaller-Muehlbacher, P. D. De Jesus, P. Teriete, M. V. Hull, M. W. Chang, J. F.-W. Chan, J. Cao, V. K.-M. Poon, K. M. Herbert, K. Cheng, T.-T. H. Nguyen, A. Rubanov, Y. Pu, C. Nguyen, A. Choi, R. Rathnasinghe, M. Schotsaert, L. Miorin, M. Dejosez, T. P. Zwaka, K.-Y. Sit, L. Martinez-Sobrido, W.-C. Liu, K. M. White, M. E. Chapman, E. K. Lendy, R. J. Glynne, R. Albrecht, E. Ruppin, A. D. Mesecar, J. R. Johnson, C. Benner, R. Sun, P. G. Schultz, A. I. Su, A. García-Sastre, A. K. Chatterjee, K.-Y. Yuen and S. K. Chanda, *Nature*, 2020, **586**, 113–119.

10 T. Muramatsu, C. Takemoto, Y.-T. Kim, H. Wang, W. Nishii, T. Terada, M. Shirouzu and S. Yokoyama, *Proc. Natl. Acad. Sci. U.S.A.*, 2016, **113**, 12997.

11 W. Dai, B. Zhang, X.-M. Jiang, H. Su, J. Li, Y. Zhao, X. Xie, Z. Jin, J. Peng, F. Liu, C. Li, Y. Li, F. Bai, H. Wang, X. Cheng, X. Cen, S. Hu, X. Yang, J. Wang, X. Liu, G. Xiao, H. Jiang, Z. Rao, L.-K. Zhang, Y. Xu, H. Yang and H. Liu, *Science*, 2020, **368**, 1331.

12 Z. Jin, X. Du, Y. Xu, Y. Deng, M. Liu, Y. Zhao, B. Zhang, X. Li, L. Zhang, C. Peng, Y. Duan, J. Yu, L. Wang, K. Yang, F. Liu, R. Jiang, X. Yang, T. You, X. Liu, X. Yang, F. Bai, H. Liu, X. Liu, L. W. Guddat, W. Xu, G. Xiao, C. Qin, Z. Shi, H. Jiang, Z. Rao and H. Yang, *Nature*, 2020, **582**, 289–293.

13 J. Chodera, A. A. Lee, N. London and F. von Delft, *Nat. Chem.*, 2020, **12**, 581.

14 A. Latorre, T. Schirmeister, J. Kesselring, S. Jung, P. Johe, U. A. Hellmich, A. Heilos, B. Engels, R. L. Krauth-Siegel, N. Dirdjaja, L. Bou-Iserte, S. Rodriguez and F. V. Gonzalez, *ACS Med. Chem. Lett.*, 2016, **7**, 1073–1076.

15 P. A. Jackson, J. C. Widen, D. A. Harki and K. M. Brummond, *J. Med. Chem.*, 2017, **60**, 839–885.

16 M. Gehringer and S. A. Laufer, *J. Med. Chem.*, 2019, **62**, 5673–5724.

17 A. Voice, G. Tresadern, H. van Vlijmen and A. Mulholland, *J. Chem. Inf. Model.*, 2019, **59**, 4220–4227.

18 R. A. Bauer, *Drug Discovery Today*, 2015, **20**, 1061–1073.

19 H. Yang, W. Xie, X. Xue, K. Yang, J. Ma, W. Liang, Q. Zhao, Z. Zhou, D. Pei, J. Ziebuhr, R. Hilgenfeld, K. Y. Yuen, L. Wong, G. Gao, S. Chen, Z. Chen, D. Ma, M. Bartlam and Z. Rao, *PLoS Biol.*, 2005, **3**, e324.

20 J. W. Keillor and R. S. Brown, *J. Am. Chem. Soc.*, 1992, **114**, 7983–7989.

21 K. Arafet, S. Ferrer and V. Moliner, *ACS Catal.*, 2017, **7**, 1207–1215.

22 K. Świderek and V. Moliner, *Chem. Sci.*, 2020, **11**, 10626–10630.

23 E. Awoonor-Williams, A. G. Walsh and C. N. Rowley, *Biochim. Biophys. Acta, Proteins Proteomics*, 2017, **1865**, 1664–1675.

24 A. Lodola, M. Mor, J. Sirirak and A. J. Mulholland, *Biochem. Soc. Trans.*, 2009, **37**, 363–367.

25 K. Arafet, S. Ferrer and V. Moliner, *Biochemistry*, 2015, **54**, 3381–3391.

26 R. E. Amaro and A. J. Mulholland, *Nat. Rev. Chem.*, 2018, **2**, 0148.

27 D. Callegari, K. E. Ranaghan, C. J. Woods, R. Minari, M. Tiseo, M. Mor, A. J. Mulholland and A. Lodola, *Chem. Sci.*, 2018, **9**, 2740–2749.

28 N. Serrano-Aparicio, K. Świderek and V. Moliner, *Eur. J. Med. Chem.*, 2019, **164**, 399–407.

29 K. Arafet, F. V. González and V. Moliner, *Chem.–Eur. J.*, 2020, **26**, 2002–2012.

30 A. Lodola, D. Callegari, L. Scalvini, S. Rivara and M. Mor, *Methods Mol. Biol.*, 2020, **2114**, 307–337.

31 L. Zhang, D. Lin, Y. Kusov, Y. Nian, Q. Ma, J. Wang, A. von Brunn, P. Leyssen, K. Lanko, J. Neyts, A. de Wilde, E. J. Snijder, H. Liu and R. Hilgenfeld, *J. Med. Chem.*, 2020, **63**, 4562–4578.

32 S. A. Gillmor, C. S. Craik and R. J. Fletterick, *Protein Sci.*, 1997, **6**, 1603–1611.

33 E. Dunny, W. Doherty, P. Evans, J. P. G. Malthouse, D. Nolan and A. J. S. Knox, *J. Med. Chem.*, 2013, **56**, 6638–6650.

34 S. Royo, S. Rodriguez, T. Schirmeister, J. Kesselring, M. Kaiser and F. V. Gonzalez, *ChemMedChem*, 2015, **10**, 1484–1487.

35 X. Zhai and T. D. Meek, *Biochemistry*, 2018, **57**, 3176–3190.

36 L. Zhu, S. George, M. F. Schmidt, S. I. Al-Gharabli, J. Rademann and R. Hilgenfeld, *Antivir. Res.*, 2011, **92**, 204–212.

37 P. S. Dragovich, T. J. Prins, R. Zhou, S. E. Webber, J. T. Marakovits, S. A. Fuhrman, A. K. Patick, D. A. Matthews, C. A. Lee, C. E. Ford, B. J. Burke, P. A. Rejto, T. F. Hendrickson, T. Tuntland, E. L. Brown, J. W. Meador, R. A. Ferre, J. E. V. Harr, M. B. Kosa and S. T. Worland, *J. Med. Chem.*, 1999, **42**, 1213–1224.

38 G. M. Torrie and J. P. Valleau, *J. Comput. Phys.*, 1977, **23**, 187–199.

39 S. Kumar, D. Bouzida, R. H. Swendsen, P. A. Kollman and J. M. Rosenberg, *J. Comput. Chem.*, 1992, **13**, 1011–1021.

40 M. J. S. Dewar, E. G. Zoebisch, E. F. Healy and J. J. P. Stewart, *J. Am. Chem. Soc.*, 1985, **107**, 3902–3909.

41 Y. Zhao and D. G. Truhlar, *Theor. Chem. Acc.*, 2008, **120**, 215–241.

42 W. J. Hehre, L. Radom, P. v. R. Schleyer and J. A. Pople, *Ab Initio Molecular Orbital Theory*, John Wiley, New York, 1986.

43 M. J. Frisch, G. W. Trucks, H. B. Schlegel, G. E. Scuseria, M. A. Robb, J. R. Cheeseman, G. Scalmani, V. Barone, B. Mennucci, G. A. Petersson, H. Nakatsuji, M. Caricato, X. Li, H. P. Hratchian, A. F. Izmaylov, J. Bloino, G. Zheng, J. L. Sonnenberg, M. Hada, M. Ehara, K. Toyota, R. Fukuda, J. Hasegawa, M. Ishida, T. Nakajima, Y. Honda, O. Kitao, H. Nakai, T. Vreven, J. A. Montgomery Jr, J. E. Peralta, F. Ogliaro, M. Bearpark, J. J. Heyd, E. Brothers, K. N. Kudin, V. N. Staroverov, R. Kobayashi, J. Normand, K. Raghavachari, A. Rendell, J. C. Burant, S. S. Iyengar, J. Tomasi, M. Cossi, N. Rega, J. M. Millam,

M. Klene, J. E. Knox, J. B. Cross, V. Bakken, C. Adamo, J. Jaramillo, R. Gomperts, R. E. Stratmann, O. Yazyev, A. J. Austin, R. Cammi, C. Pomelli, J. W. Ochterski, R. L. Martin, K. Morokuma, V. G. Zakrzewski, G. A. Voth, P. Salvador, J. J. Dannenberg, S. Dapprich, A. D. Daniels, O. Farkas, J. B. Foresman, J. V. Ortiz, J. Cioslowski, and D. J. Fox, *Gaussian 09 (Revision A.1)*, 2009.

44 K. Świderek, I. Tuñón, S. Martí and V. Moliner, *ACS Catal.*, 2015, **5**, 1172–1185.

45 K. Świderek, I. Tuñón, V. Moliner and J. Bertran, *ACS Catal.*, 2015, **5**, 2587–2595.

46 A. Krzemińska, V. Moliner and K. Świderek, *J. Am. Chem. Soc.*, 2016, **138**, 16283–16298.

47 Y. Duan, C. Wu, S. Chowdhury, M. C. Lee, G. Xiong, W. Zhang, R. Yang, P. Cieplak, R. Luo, T. Lee, J. Caldwell, J. Wang and P. Kollman, *J. Comput. Chem.*, 2003, **24**, 1999–2012.

48 W. L. Jorgensen, J. Chandrasekhar, J. D. Madura, R. W. Impey and M. L. Klein, *J. Chem. Phys.*, 1983, **79**, 926–935.

49 M. J. Field, M. Albe, C. Bret, F. Proust-De Martin and A. Thomas, *J. Comput. Chem.*, 2000, **21**, 1088–1100.

50 R. A. Friesner, J. L. Banks, R. B. Murphy, T. A. Halgren, J. J. Klicic, D. T. Mainz, M. P. Repasky, E. H. Knoll, M. Shelley, J. K. Perry, D. E. Shaw, P. Francis and P. S. Shenkin, *J. Med. Chem.*, 2004, **47**, 1739–1749.

51 J. R. A. Silva, L. Cianni, D. Araujo, P. H. J. Batista, D. de Vita, F. Rosini, A. Leitao, J. Lameira and C. A. Montanari, *J. Chem. Inf. Model.*, 2020, **60**, 1666–1677.

52 A. Paasche, A. Zipper, S. Schäfer, J. Ziebuhr, T. Schirmeister and B. Engels, *Biochemistry*, 2014, **53**, 5930–5946.

53 C. A. Ramos-Guzmán, J. J. Ruiz-Pernía and I. Tuñón, 2020, DOI: 10.26434/chemrxiv.12895064.v1.

54 J. Singh, R. C. Petter, T. A. Baillie and A. Whitty, *Nat. Rev. Drug Discovery*, 2011, **10**, 307–317.